Nuclear Analysis of the DEMO Divertor Survey Visible High-Resolution Spectrometer

R. Luís[1], Y. Nietiadi[1], A. Silva[1], B. Gonçalves[1], T. Franke[2,3], W. Biel[4,5]

[1] *Instituto de Plasmas e Fusão Nuclear, Instituto Superior Técnico, Universidade de Lisboa, Portugal*

[2]*Max-Planck-Institut für Plasmaphysik, Garching, Germany*

[3]*EUROfusion Power Plant Physics and Technology (PPPT) department, Garching, Germany*

[4]*Institut für Energie und Klimaforschung, Forschungszentrum Jülich GmbH, Germany*

[5]*Department of Applied Physics, Ghent University, Belgium*

Spectroscopic measurements have been recently proposed in DEMO for divertor detachment control. In its current design, the DEMO Divertor Survey Visible High-Resolution Spectrometer is foreseen to perform spectroscopy measurements by integrating three optical subsystems into an equatorial port (EP). Behind the first wall, light travels through a set of metallic mirrors and ducts before it reaches the closure plate of the EP. This paper presents a nuclear analysis performed with the Monte Carlo simulation program MCNP6 for two alternative configurations of the system. The results show that the configuration with 5 mirrors per transmission line is very effective to reduce the neutron streaming through the port. However, it will not be possible, with the current design, to introduce standard electronics along the spectroscopy ducts, as the dose rate limits for non-critical electronic components are exceeded in both configurations. In the plasma-facing mirrors, the heat loads are below 2 mW/cm^3, which shows that the strategy of recessing the first mirrors and placing them behind small-diameter openings is effective to decrease the loads in the mirrors. FISPACT simulations for different materials show that material transmutation in the mirrors will be negligible throughout the DEMO reactor lifetime.

Keywords: DEMO; Neutronics; Spectroscopy; Transmutation; MCNP

1 Introduction

A preliminary set of diagnostics and control (D&C) systems has been recently proposed for the future tokamak demonstration fusion reactor (DEMO) [1]. Due to the higher radiation loads in the plasma-facing components and the need for tritium breeding [2], the integration of these systems in DEMO is subjected to constraints which go far beyond the ones currently faced in ITER. Therefore, the proposed D&C system is constantly evolving, with the aim to select and develop diagnostics with the robustness and reliability required for plasma control in the harsh radiation environment foreseen for DEMO.

In particular, divertor spectroscopic measurements have been recently proposed as a control method for the detachment of the divertor plasma [3]. As schematized in Figure 1, the DEMO Divertor Survey Visible (VIS) High-Resolution (HR) Spectrometer is foreseen to perform spectroscopic measurements by integrating three optical subsystems into an equatorial port (EP), inspecting the outer, x-point and inner divertor regions under oblique angles with a set of sightlines that are almost parallel to the target [4]. Behind the first wall, the light travels through a set of metallic mirrors and ducts before it reaches the closure plate of the EP. A first design proposed for this system is represented in Figure 2.

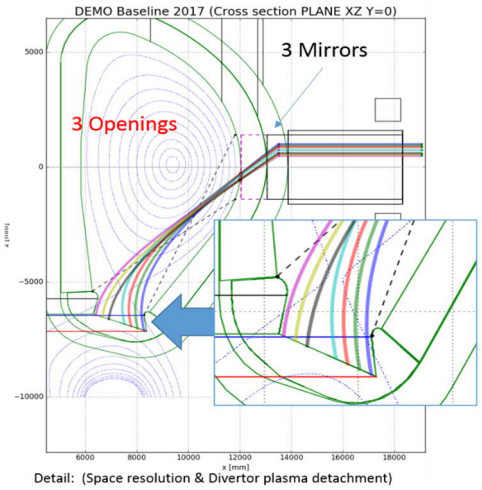

Figure 1: Lines of sight of the DEMO Divertor Survey VIS HR Spectrometer, projected into a poloidal plane[1].

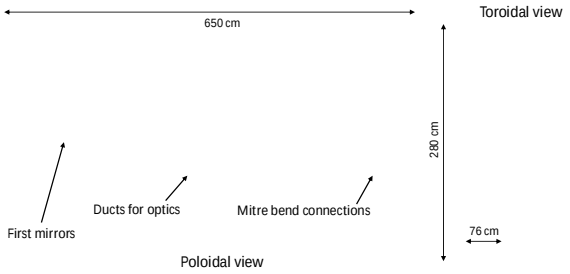

Figure 2: Schematic model of the DEMO Divertor Survey VIS HR Spectrometer.

[1] Since the lines of sight are inclined in both the toroidal and poloidal directions, their projections in the poloidal plane are curved.

Corresponding author: rluis @ipfn.tecnico.ulisboa.pt

The objective of this work was to perform a nuclear analysis for two alternative configurations of the DEMO Divertor Survey VIS HR spectrometer, using the Monte Carlo simulation program MCNP6 [5]. The CAD model of the first configuration is represented in Figure 3. To reduce the radiation loads in the first mirrors and prevent material transmutation, the first mirrors are recessed from the first wall, behind ducts with an approximate length of 2 m. The openings in the first wall are ellipses with short radii of ~3.5 cm and long radii of ~5 cm, which increase progressively towards the plasma-facing mirrors. In this configuration there is only one mirror per transmission line, which means that light coming from the divertor is reflected in this mirror and travels directly to the back of the equatorial port without further reflections. Since there is only one mirror per transmission line, this configuration will be referred to as the 1-mirror configuration.

Figure 3: CAD model of the 1-mirror configuration (1 mirror per transmission line).

The second configuration is represented in Figure 4. This is the 5-mirror configuration, since in each transmission line there are five mirrors between the plasma and the closure plate of the EP, with the aim of reducing the neutron streaming through the port. The mirrors have different volumes and are connected by ducts of variable radius. The openings in the first wall are the same as in the 1-mirror case.

Figure 4: CAD model of the 5-mirror configuration (5 mirrors per transmission line).

Both configurations are designed to occupy one drawer of an ITER-like equatorial port containing three drawers for diagnostics, although the ducts from the first wall to the first mirrors are tilted in the toroidal direction and will impose restrictions on the design of diagnostics in the neighbouring drawers. The equatorial port model assumed for this work is a generic one, included in the reference model used for the neutronics simulations (see section 2.1) [6]. The total length of each system, from the first wall to the back of the port, is 6.5 meters. Although other configurations (3 mirrors, 7 mirrors, 9 mirrors) are also possible, these two designs were deemed as adequate to evaluate the effect of the number of mirrors per duct on the neutron streaming through the port.

2 Simulation methods

For the nuclear analysis, the CAD models presented in the previous section were simplified using ANSYS Spaceclaim [7] and converted to the MCNP input format using the CAD-based modelling program SuperMC [8,9]. The neutronics simulations were performed using the Monte Carlo simulation program MCNP6.1 with FENDL 2.1 [10] and FENDL 3.1 [11] cross sections, after the implementation of the converted model in a 22.5-degree DEMO neutronics reference model [6]. As this model is generic (i.e., it can be adapted to any blanket configuration), the Breeding Blankets (BB) were filled with a homogeneous mixture based on the latest design of the Water-Cooled Lithium Lead (WCLL) BB [12]. All the simulations were performed in the high-performance computer MARCONI-FUSION [13].[13]

2.1 MCNP models

The MCNP models of the two configurations are presented in Figure 5 and Figure 6. In both models, the plasma-facing component (grey), with 6 cm of thickness, was filled with a homogeneous mixture of 83.2 % tungsten, 5.5%, water and 11.3% CuCrZr, while the shield block behind it (light blue), with a minimum thickness of 42 cm, was filled with a mixture of 87.5% EUROFER, 7.4% water and 5.1% void. The remaining structure was filled with stainless steel (green), except for the mirrors, filled by EUROFER (pink) as bulk material in the main configuration. Besides EUROFER, five additional materials were tested in the mirrors, both as bulk materials and as surface coating: gold, platinum, molybdenum, rhodium and tungsten (more details in section 3.4 below).

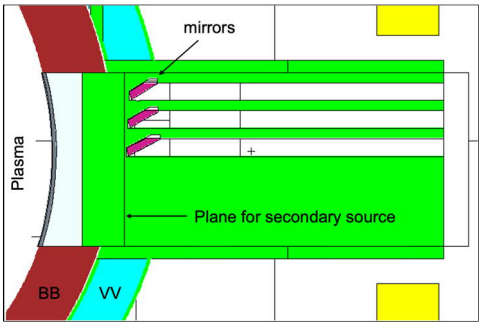

Figure 5: MCNP model of the 1-mirror configuration.

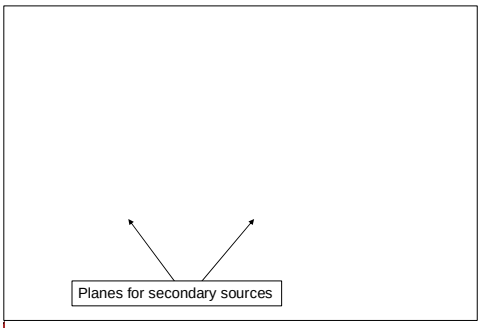

Figure 6: MCNP model of the 5-mirror configuration.

2.2 Variance reduction techniques

The most difficult challenge in deep-penetration problems such as the one presented here is to obtain reliable

simulation results at large distances from the neutron source. In this case, the back part of the spectroscopy system is 6.5 meters away from the first wall, or almost 10 meters away from the centre of the plasma. A typical MCNP simulation with 2E9 source particles (~24h with 400 processors) without variance reduction will have very poor statistics in the first mirrors, which are located at just 1.2 meters from the first wall. Therefore, it is mandatory to employ variance reduction techniques in the simulations. To this effect, the Automated Variance Reduction Generator (ADVANTG) [14] software was used to generate weight windows for variance reduction. Several sets of weight windows were tested (with different bin sizes and input parameters, optimized for tallies at different locations, etc.) through trial and error to find the ones best suited to the problem. Even though it was possible to obtain satisfactory results for the 1-mirror configuration, for the 5-mirror configuration none of the tested weight window meshes was sufficient to have any particle tallied at the closure plate. A different strategy was then adopted for the simulations, which consisted in introducing planes to split the geometry into two (1-mirror configuration) or three (5-mirror configuration) parts and use the weight windows produced with ADVANTG along with *ssw* cards to record secondary sources on these planes (also represented in Figure 5 and Figure 6). Using as example the 1-mirror configuration, in a simulation with 2E9 source particles approximately 8E5 histories were recorded on this plane. The resulting secondary source, with neutrons and gammas, was then employed in a second simulation to obtain the fluxes in the remaining part of the spectroscopy system. A multiplication factor of 1000 was used for this secondary source, meaning that each recorded particle was sampled 1000 times with different random number seeds. This is "equivalent" to running 2E12 source particles in one simulation.

The neutron fluxes at the exit of the ducts in the 1-mirror configuration are summarized in Table 1 for two cases: 1) a single simulation using "hard" weight windows (with the highest weight ~70 orders of magnitude higher than the lowest weight) and 2) a two-step simulation using "soft" weight windows (with the highest weight ~13 orders of magnitude higher than the lowest weight) and a secondary source recorded in the plane represented in Figure 5. The secondary source method produces lower statistical errors, below 3.5% for the three cases. It is also important to notice that the results obtained with these two methods are in excellent agreement for the middle and bottom ducts, while for the duct on the top there is a 28% deviation between the two methods. Since the neutron flux from the plasma to the back of the equatorial port is reduced by more than 5 orders of magnitude, this deviation between the two simulation methods is relatively small.

The method with the secondary source was chosen for the remainder of this work, since it yields the lowest statistical errors while reducing significantly the computational time per simulation. This is in part because the "hard" weight window mesh produces long histories, which dramatically reduce the efficiency of the parallel simulations. Although there are software tools that can be used to soften the weight windows, the softened weight windows obtained with these tools were never sufficiently effective to produce the desired results. The solution found to overcome this problem was to further tune the weight windows while adapting the location of the secondary source according to the region of interest in each simulation.

Table 1 – Neutron fluxes at the exit of the ducts for two different simulation approaches (1-mirror configuration).

Line	Hard Weight Windows		Sec. Source	
	Neutron flux (1/cm^2/s)	Stat. Error (%)	Neutron flux (1/cm^2/s)	Stat. Error (%)
Top	1.1E+09	7.2	7.9E+08	3.3
Middle	1.6E+09	5.2	1.5E+09	3.0
Bottom	1.8E+09	8.6	1.9E+09	1.9

The two surfaces added to the 5-mirror configuration to generate the secondary source are represented in Figure 6: the first is located just before the mirrors, while the second is located close to the middle of the system. In this way, a first simulation records neutrons on the first plane (on the left), and a second simulation is used to tally neutrons and gammas in first three mirrors of each sightline. To score neutrons at the exit of the pipes, the first simulation is re-run, now with weight windows optimized to score the secondary source on the second plane (on the right), and the second simulation is re-run to propagate these neutrons to the exit of the pipes. In total, 4 simulations are required to obtain results with acceptable statistical errors in the whole spectroscopy system.

Each of these simulations is run with a different set of weight windows, optimized individually for each case. The weight windows used to tally neutrons at the exit of the ducts are shown in Figure 7. The ones from simulation 1 are optimized to the region of the secondary source plane in the middle of the spectroscopy system, while the ones from simulation 2 are optimized to the region at the exit of the ducts. The latter had to be adjusted to the average weight of the secondary source particles (a custom SDEF source was used to produce them) and softened using the iWW-GVR tool [15]. The results of the simulations have different normalizations, according to the number of secondary source particles sampled in each case.

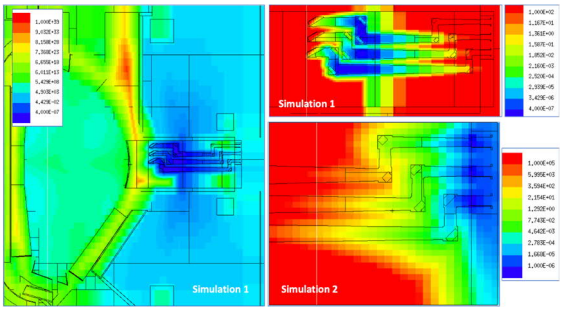

Figure 7: Weight windows generated in ADVANTG to obtain results at the exit of the ducts.

3 Results and discussion

3.1 Neutron and gamma fluxes in the system

The neutron fluxes in both configurations are presented in Figures 8 and 9. In the 1-mirror configuration, the plot joins results from two simulations: 1) with the plasma neutron source and 2) with the secondary source. In the 5-mirror configuration, the plot joins results from three simulations: 1) with the plasma neutron source, 2) with the secondary source generated in the left-side plane of Figure 6 and 3) with the secondary source generated in the right-side plane of Figure 6.

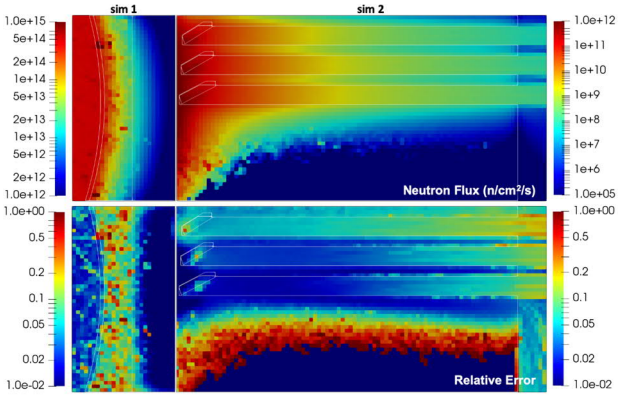

Figure 8: Neutron fluxes (n/cm^2/s) in the 1-mirror configuration. The plots merge results from two simulations (the second was run with a secondary source).

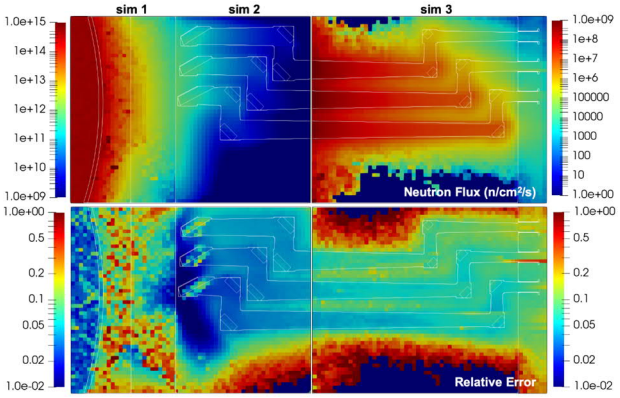

Figure 9: Neutron fluxes (n/cm^2/s) in the 5-mirror configuration. The plots merge results from three simulations (two of which run with secondary sources).

The separations in the figures indicate the places where the plots are joined. As the fluxes span several orders of magnitude, two scales were used in each plot, to improve the readability of the results. For both cases, the highest neutron flux at the exit of the ducts is in the bottom duct, reaching 1.5E+08 n/cm^2/s in the 1-mirror configuration and close to 1.0E+05 in the 5-mirror configuration. This means that the 5-mirror configuration is very effective to reduce the neutron streaming to the back of the equatorial port, decreasing the neutron fluxes by more than 3 orders of magnitude when compared to the 1-mirror configuration. It is more effective in the top duct than in the remaining ones, and much less effective in the bottom duct, since at the location of the fourth mirror a fraction of the neutrons travelling across the top and middle ducts crosses the small thickness of stainless steel that separates them from the duct below. Therefore, in order to make the system more effective from the neutron shielding point of view, this thickness should be increased, by decreasing the length of the ducts that separate the third and fourth mirrors of the middle and bottom ducts.

The statistical errors (also presented in Table 2) in the total fluxes at the exit of the ducts are between 2% and 7.5% for the 1-mirror configuration and between 6 to 18% for the 5-mirror configuration. Considering that the fluxes span more than 10 orders of magnitude in the 5-mirror configuration, these results show the effectiveness of the strategy employed in the simulations. The errors in each bin are even smaller in the 5-mirror configuration than in the 1-mirror configuration; such small errors were only possible by sampling each particle scored in the mid-plane 10^4 times, which is "equivalent" to running 2E13 source particles in the first simulation. The relatively large statistical errors in the plasma-facing components are justified by the weight windows, which are optimized by ADVANTG to propagate the neutrons through the lines of sight of the spectroscopy system.

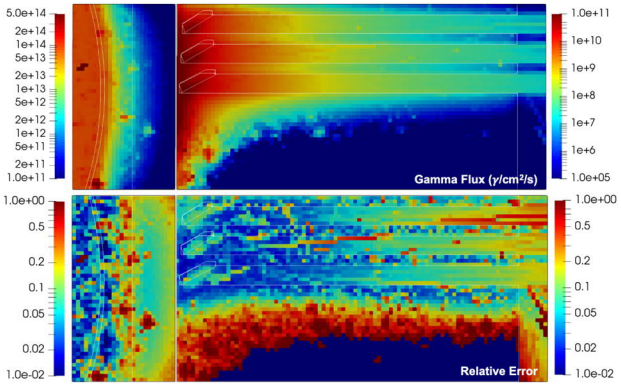

Figure 10: Gamma fluxes (γ/cm^2/s) in the 1-mirror configuration.

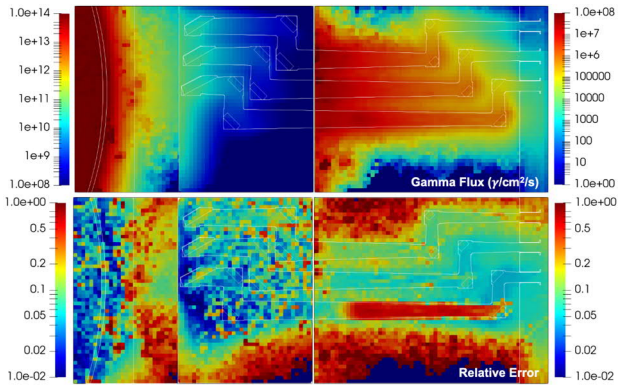

Figure 11: Gamma fluxes (γ/cm^2/s) in the 5-mirror configuration.

The gamma fluxes for both configurations are presented in Figures 10 and 11. In this case the statistical errors are larger, since it was not possible, due to the increased simulation times, to optimize the weight windows for gammas in the same way as they were optimized for neutrons. Therefore, the gammas reaching the exit of the ducts are produced locally, through the interaction of neutrons with the surrounding materials.

Table 2 – Neutron and gamma fluxes at the exit of the ducts.

Line	1-mirror				5-mirror			
	Neutron flux (n/cm²/s)	Stat. Error (%)	Gamma flux (γ/cm²/s)	Stat. Error (%)	Neutron flux (n/cm²/s)	Stat. Error (%)	Gamma flux (γ/cm²/s)	Stat. Error (%)
Top	6.97E+07	7.42	1.45E+07	10.6	1.64E+03	18.2	3.16E+02	15.5
Middle	1.24E+08	2.80	2.33E+07	6.17	2.40E+04	12.5	2.80E+03	7.10
Bottom	1.51E+08	2.38	2.68E+07	4.43	9.70E+04	6.01	1.46E+04	4.69

This does not, in general, lead to a sizable underestimation of the gamma fluxes, as the gammas coming from the materials surrounding the plasma have a small contribution to the fluxes in distant regions. Once again, the 5-mirror configuration leads to much lower fluxes than the 1-mirror configuration. The large statistical errors are visible mostly along the pipe connecting mirrors 3 and 4 of the lower duct.

3.2 Dose rates during operation

The ambient dose equivalent rates during operation were also calculated, by multiplying the neutron and gamma fluxes by flux-to-dose conversion factors [16]. As shown in Figure 12 and Figure 13, the dose rates at the exit of the pipes reach 10 Sv/h in the 1-mirror configuration and 5 mSv/h in the 5-mirror configuration. As the equivalent dose rates are dominated by neutrons, the statistical errors are small all along the ducts.

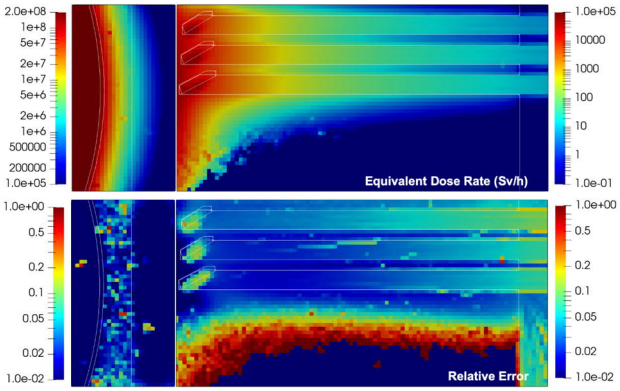

Figure 12: Ambient dose equivalent rates (Sv/h) during operation in the 1-mirror configuration.

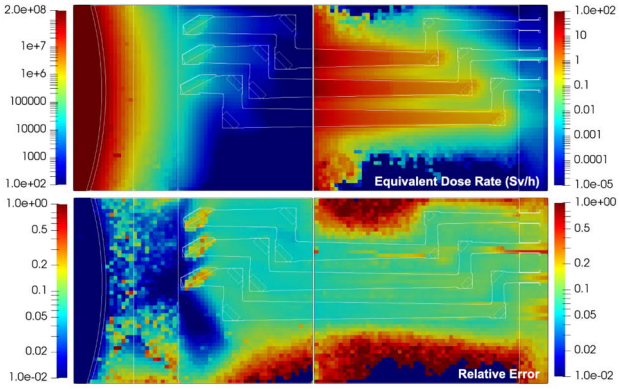

Figure 13: Ambient dose equivalent rates (Sv/h) during operation in the 5-mirror configuration.

More important is the absorbed dose in silicon, presented in Figure 14 and Figure 15, which allows to estimate the location where it becomes possible to introduce electronics in the system. These estimations were obtained using FMESH flux tallies for neutrons and gammas multiplied by the total cross sections and the average heating number (MeV/collision) for silicon. As the dose rate in silicon is dominated by gammas, the statistical errors are larger, most notably in the bottom duct of the 5-mirror configuration. In the 1-mirror configuration, the absorbed dose in silicon during one Full-Power Year (FPY) reaches 2E6 Gy, while in the 5-mirror configuration it reaches ~50 Gy/FPY in the bottom duct and ~1 Gy/FPY in the top one. According to the exposure limits established for ITER, the accumulated dose in electronics for non-critical components shall not exceed 10 Gy, while the neutron fluence shall not exceed 100 n/cm²/s [17]. With the current estimation, the accumulated dose in electronics at the exit of the top duct in the 5-mirror configuration would not exceed the limit, either during the first or the second operation stages of DEMO (1.57 and 4.43 FPY, respectively). However, the neutron fluxes exceed the limit by more than one order of magnitude, even in the top duct. This means that unless further measures are taken to reduce the neutron fluxes, standard electronics cannot not be placed anywhere along the spectroscopy ducts. Furthermore, the current simulations are not taking into account the contributions from other diagnostics and ports to the radiations levels at the back of the equatorial port, which can contribute to increase de dose rates at the exit of the spectroscopy system.

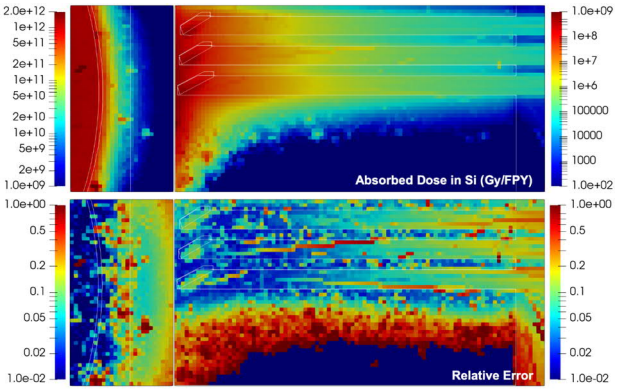

Figure 14: Dose rates (Gy/FPY) in silicon during operation in the 1-mirror configuration.

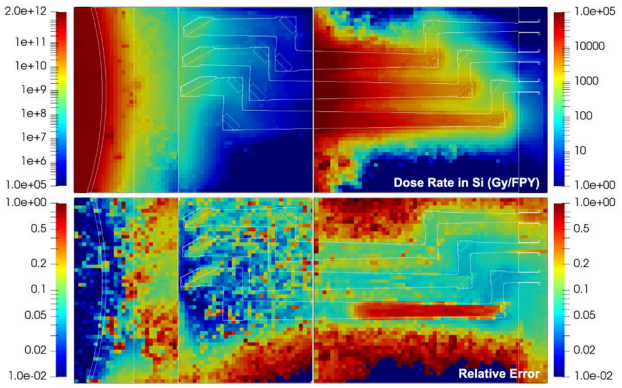

Figure 15: Dose rates (Gy/FPY) in silicon during operation in the 5-mirror configuration.

3.3 *Fluxes and heat loads in the mirrors*

After studying the radiation levels across the whole system, the fluxes and heat loads in the mirrors were considered. Figure 16 shows the neutron flux spectra in the first mirrors. Due to the large number of energy bins (175), there are large uncertainties in some parts of the spectra, mainly in the low- and high-energy regions (below 10 eV and above 100 keV). The mirror with the highest flux is the bottom mirror, with a total flux of 1.85E11 n/cm^2/s, as presented in Table 3 (mirror 11), in which the mirrors are numbered from 1 (first mirror in the top duct) to 15 (last mirror in the bottom duct). This is more than three orders of magnitude lower than the neutron flux at the first wall. As also shown in Table 3, the maximum gamma flux in the mirrors is 2.4E10 γ/cm2/s, while the heat loads in the first mirrors range from 0.1 to 0.14 mW. The remaining mirrors have even lower loads.

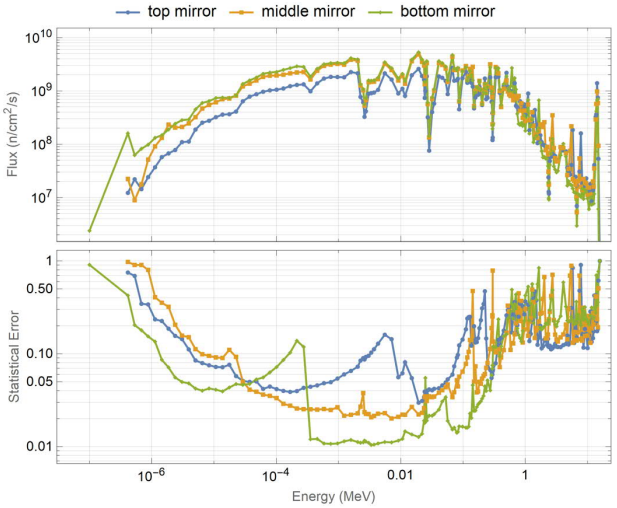

Figure 16: Neutron flux spectra (n/cm^2/s) in the first mirrors, for the 5-mirror configuration.

3.4 *Alternative materials for the first mirrors*

In the previous simulations, EUROFER was the bulk material used in the mirrors. Five additional candidate materials were tested: gold, tungsten, platinum, molybdenum and rhodium. Under "clean room conditions" one would simply look for the material with the highest reflectivity, but in DEMO additional criteria like the behaviour under irradiation, resilience against erosion and resilience against steam ingress have to be considered. From the materials discussed in this section, rhodium has been proposed for optical diagnostics in ITER [18], while single crystalline molybdenum has also been shown to be very resilient against erosion [19]. As such analyses have not been completed yet for DEMO, the five previously mentioned high-Z metallic materials were chosen for comparison. It is important to underline that eventual losses along the optical lines depend on the mirror material and need to be further evaluated in spectroscopic simulations.

In a first stage, even though it may be unrealistic in some cases, the 5 candidates were tested as bulk materials (Table 4). In a second stage, they were tested as a thin coating at the surface of the mirror (Table 5). The results presented in this section refer to the first mirror of the bottom duct, as it is the one with the highest neutron fluxes and the largest mass.

Table 3: Fluxes and heat loads in the mirrors (5-mirror configuration).

LOS	Mirror	Neutron flux (n/cm^2/s)	Error (%)	Gamma flux (γ/cm^2/s)	Error (%)	Heat Load (W/cm^3)	Error (%)
Top	1	1.18E+11	5.4	1.95E+10	6.5	1.09E-04	6.9
	2	2.83E+09	3.9	4.16E+08	3.7	2.33E-06	3.1
	3	1.66E+09	4.2	2.56E+08	6.6	1.52E-06	7.1
	4	9.28E+06	6.9	1.00E+06	11	6.04E-09	11
	5	5.76E+05	7.5	8.99E+04	9.3	5.38E-10	9.4
Middle	6	1.76E+11	3.6	2.44E+10	5.6	1.44E-04	6.5
	7	1.10E+10	3.3	1.66E+09	2.1	9.48E-06	2.1
	8	4.92E+09	3.5	7.01E+08	2.5	4.13E-06	2.6
	9	9.07E+06	5.8	8.56E+05	5.5	5.27E-09	5.6
	10	7.84E+05	6.0	1.14E+05	5.2	6.77E-10	5.1
Bottom	11	1.85E+11	3.0	2.41E+10	5.6	1.41E-04	6.6
	12	3.34E+10	2.4	4.85E+09	2.4	2.88E-05	3.7
	13	6.79E+09	2.9	1.02E+09	2.6	6.07E-06	3.0
	14	4.88E+06	4.6	6.55E+05	16	3.92E-09	14
	15	5.32E+05	6.0	8.05E+04	4.5	4.75E-10	4.5

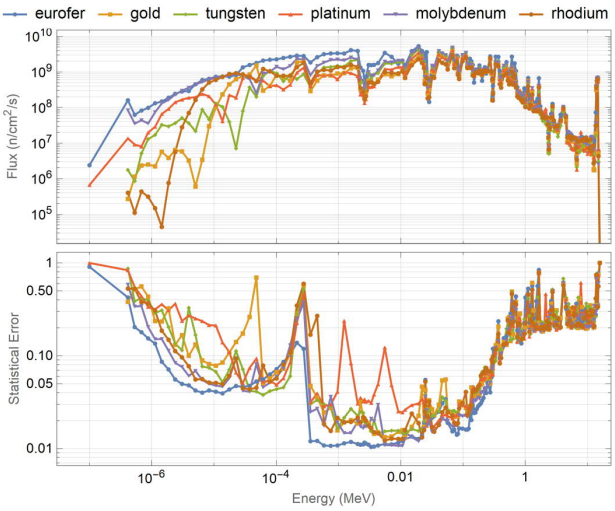

Figure 17: Neutron flux spectra (n/cm^2/s) in the first mirror of the bottom duct, for 6 alternative materials.

The neutron flux spectra across the six bulk materials are presented in Figure 17. These spectra were used as input in the inventory code FISPACT [20] to estimate the displacements per atom (dpa), the gas production and the material transmutation in the mirrors, using JEFF 3.3 libraries [21]. The results are presented in Table 4, along with the heat loads by prompt neutrons and gammas calculated with MCNP. For most materials, more than 90% of the heat loads is energy deposited by gammas, except for rhodium, where the lower energy deposition by gammas results in a lower heat load compared to the remaining materials. The highest heat load by prompt neutrons and gammas is in molybdenum, although it is still below 0.3 W/cm^3.

It is important to notice that besides the nuclear heat loads by prompt neutrons and gammas, the decay heat may also play an important role during operation, depending on the material. The most evident case is that of rhodium, since natural rhodium consists of the single isotope ^{103}Rh which under irradiation transmutes by neutron capture to ^{104}Rh. This isotope is unstable and undergoes beta decay (with a half-life of 42.3 seconds) to stable ^{104}Pd, with additional gamma de-excitation. As such, the beta decay of ^{104}Rh, with a maximum beta energy of 2.44 MeV (and an average of 0.985 MeV) [22], contributes significantly to the nuclear heat loads during plasma operation. In recent studies performed for ITER diagnostics, it was estimated that the decay heat in rhodium for plasma-facing mirrors can be more than 20 times higher when compared to the heat loads by prompt neutrons and gammas [23]. To evaluate the decay heat in rhodium as a function of the operation time, additional FISPACT simulations were run. The results are shown in Figure 18, for the first 400 seconds of operation. After less than 5 minutes the decay heat is already converging to ~1.8 mW/cm^3, which is a factor ~28 higher than the estimated value for prompt neutrons and gammas, in agreement with the estimations for ITER provided in reference [23]. Therefore, it is mandatory to include the decay heat contribution in all the thermal assessments performed for rhodium mirrors.

Similar calculations were done for the remaining materials, and the only one in which the decay heat eventually surpasses the heat loads by prompt neutrons and gammas is gold, as shown in Figure 19. In this case, the only natural occurring isotope is ^{197}Au. This isotope transmutes by neutron capture to ^{198}Au, which then undergoes beta decay to stable ^{198}Hg with a half-life of 2.69 days and additional gamma de-excitation [24]. As shown in Figure 19, the decay heat when the mirror material is gold converges to 1.6 mW/cm^3 after ~10 days of operation (DEMO is foreseen to operate in 120-minute cycles with 10 minutes of down time [25]), a factor 8 higher than the estimated value for prompt neutrons and gammas.

In tungsten the decay heat after a few days of operation will be comparable to the value estimated for prompt neutrons and gammas, while in the remaining materials the decay heat contribution is smaller.

The dpa values and the H and He production (Table 4) are very small for all materials, and material transmutation is negligible in all cases (1.54 g of Hg-198 are produced in gold in a full power year, which corresponds to 0.001% of the total weight of the mirror). This means that, taking into account the location of the first mirrors in the current configuration, material transmutation should not be a cause for concern.

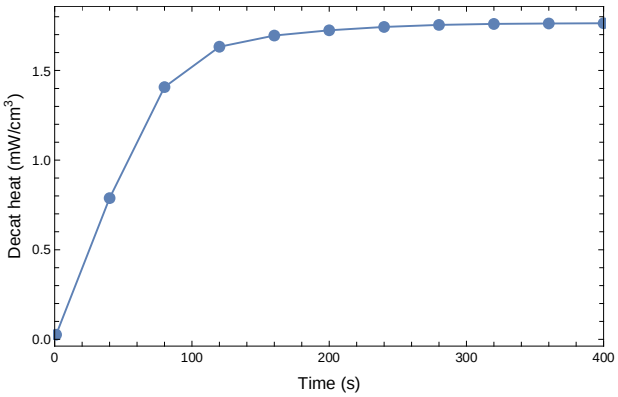

Figure 18: Decay heat in a rhodium mirror (first mirror of the bottom duct) as a function of the operation time.

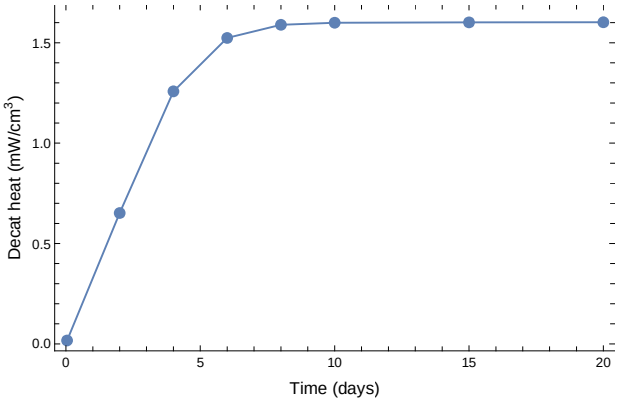

Figure 19: Decay heat in a gold mirror (first mirror of the bottom duct) as a function of the operation time.

For the surface coating, a F2 tally was used to score the neutron fluxes at the front surface of the EUROFER mirror and this flux was used in FISPACT with the six materials considered before. The mass used in each case is the surface area of the mirror multiplied by 0.1 mm of thickness and by the material density. In every case, as shown in Table 5, the conclusion is the same as before: the dpa values are small and the material transmutation is negligible. To have an estimation of how the material transmutation depends on the intensity of the neutron flux, the FISPACT simulations were repeated for three cases, with the nominal flux multiplied by 10, 100 and 1000. This corresponds crudely to three configurations in which the mirrors are brought successively closer to the plasma (or in which the radii of the first wall openings increase), until the flux is close in magnitude to the neutron flux in the first wall. Although this is a very conservative estimation, it can be useful as reference if for some reason the strategy of recessing the mirrors by more than 2 meters from the first wall is reversed in the future. As before, gold is the material in which more transmutation occurs: 1.6% of the original weight when the flux is multiplied by 100 and 14.6% when the flux is multiplied by 1000. In the remaining materials, transmutation plays a much smaller role.

Table 4: Nuclear heat loads (by prompt neutrons and gammas, calculated with MCNP), dpa, gas production and transmutation (calculated with FISPACT) in the first mirror of the bottom duct, for 6 bulk materials.

Material	Mass (kg)	Heat Load (mW/cm^3)	dpa (/FPY)	Initial Composition	Composition (1 FPY)	He (appm/FPY)	H (appm/FPY)
Eurofer	85.4	0.141 (92.9% by gammas)	6.9E-04	88.8% Fe 9% Cr 1.1% W others: 1.1%	88.8% Fe 9% Cr 1.1% W others: 1.1%	4.0E-03	1.2E-02
W	210.7	0.147 (99.4% by gammas)	3.0E-04	100% W	100% W others: 0.22 g	4.5E-05	1.5E-04
Au	211.5	0.195* (93.3% by gammas)	5.1E-04	100% Au	99.999% Au others: 1.56 g (1.54 g Hg-198)	1.2E-05	8.3E-05
Pt	234.8	0.182 (99.2% by gammas)	6.6E-04	100% Pt	100% Pt others: <0.1 g	2.7E-05	1.2E-04
Rh	135.8	0.064* (56.9% by gammas)	6.0E-04	100% Rh	100% RH others: 0.66 g (0.65 g Pd-104)	4.8E-04	3.0E-03
Mo	111.9	0.277 (98.2% by gammas)	5.2E-04	100% Mo	100% Mo others: <0.06 g	7.8E-04	9.3E-03

**in Rh and Au the decay heat will exceed the heat by prompt neutrons and gammas after short operation periods. Decay heat values of ~ $2mW/cm^3$ were estimated with FISPACT after 5 minutes (Rh) and 10 days (Au) of operation, respectively.*

Table 5: Transmutation in the first mirror of the bottom duct, for 6 coating materials.

Material	Initial Composition	Composition (1 FPY)			
		Nominal flux	Flux * 10	Flux * 100	Flux * 1000
Eurofer	88.8% Fe 9% Cr 1.1% W others: 1.1	88.8% Fe 9% Cr 1.1% W others: 1.1%	88.8% Fe 9% Cr 1.1% W others: 1.1%	88.8% Fe 9% Cr 1.1% W others: 1.1%	88.8% Fe 9% Cr 1.1% W others: 1.1%
W	100% W	100% W others: 5.2 mg	99.98% W others: 52 mg	99.75% W others: 0.52 g	99.62% W others: 5.0 g
Au	100% Au	99.98% Au others: 33 mg (33 mg Hg-198)	99.84% Au others: 0.33 g (0.33 g Hg-198)	98.43% Au others: 3.3 g (3.3 g Hg-198)	85.40% Au others: 30.9 g (30.5 g Hg-198)
Pt	100% Pt	100% Pt others: 0.45 mg	100% Pt others: 4.5 mg	99.98% Pt others: 0.05 g	99.81% Pt others: 0.46 g
Rh	100% Rh	100% RH others: 5.2 mg (5.2 mg Pd-104)	99.96% RH others: 52 mg (52 g Pd-104)	99.62% RH others: 0.5 g (0.5 g Pd-104)	96.26% RH others: 5.1 g (5.0 g Pd-104)
Mo	100% Mo	100% Mo others: 0.1 mg	100% Mo others: 1 mg	99.99% Mo others: 10 mg	99.91% Mo others: 0.1 g

4 Conclusions

In this paper, two alternative configurations of the DEMO Divertor Survey VIS HR Spectrometer were studied in detail, with the aim of assessing the effects of neutron and gamma radiation on the first mirrors and the effect of the number of mirrors on the neutron streaming through the equatorial port. The simulations have shown that the 5-mirror configuration is very effective to reduce the neutron streaming to the back of the EP, decreasing the neutron fluxes by more than 3 orders of magnitude when compared to the 1-mirror configuration. A similar reduction is seen in the gamma fluxes and dose rates. It should not be possible, however, to introduce electronics along the spectroscopy ducts. Although the accumulated dose in silicon at the exit of one of the ducts would not exceed the limit of 10 Gy foreseen for non-critical components in ITER, the neutron fluxes would exceed 100 n/cm^2/s by more than one order of magnitude in any of the ducts. This means that unless further measures are taken to reduce the neutron fluxes, standard electronics cannot not be placed anywhere in the spectroscopy ducts. In future studies, the methodology set out in this paper to calculate the neutron and gamma streaming through the EP shall be employed to evaluate alternative shielding configurations, with the aim of reducing the fluxes in the closure plate while decreasing, if possible, the total mass of the EP.

In the first mirrors, the heat loads by prompt neutrons and gammas with the current configuration are below 0.3 mW for all the tested materials, with neutron fluxes of ~2E11 n/cm^2/s. Under these neutron fluxes, significant material transmutation is not expected to occur. However, for some mirror materials, most notably rhodium but also for gold, the decay heat will exceed the heat by prompt neutrons and gammas after short operation periods, reaching values up to ~ 2 mW/cm^3 which must be taken into consideration in future thermal analyses. Nevertheless, the results presented in this paper show that the strategy adopted in DEMO of recessing the plasma-facing components of diagnostics systems from the first wall will be effective to protect the mirrors against material transmutation and radiation damage. They will also serve as reference for the study of other spectroscopy systems to be considered for the DEMO equatorial ports.

Acknowledgments

This work has been carried out within the framework of the EUROfusion Consortium and has received funding from the Euratom research and training programme 2014-2018 and 2019-2020 under grant agreement No. 633053. The reviews and opinions expressed herein do not necessarily reflect those of the European Commission.

References

[1] W. Biel et al. Diagnostics for plasma control – From ITER to DEMO, Fusion Engineering and Design 146 (2019) 465–472

[2] G. Federici et al. An overview of the EU breeding blanket design strategy as an integral part of the DEMO design effort, Fusion Engineering and Design 141 (2019) 30-42

[3] W. Gonzalez et al. Conceptual studies on spectroscopy and radiation diagnostic systems for plasma control on DEMO, Fusion Engineering and Design 146-B (2019) 2297-2301

[4] W. Gonzalez et al. Preliminary study of a visible, high spatial resolution spectrometer for DEMO divertor survey, Journal of Instrumentation 15 (2020) C01008

[5] G. W. McKinney, F. B. Brown, et al., "MCNP 6.1.1 New Features Demonstrated", IEEE 2014 Nuclear Science Symposium, Seattle, Nov 8-15, LA-UR-14-23108 (2014)

[6] ANSYS® Academic Associate, v19.0

[7] Y. Li et al. *"Benchmarking of MCAM 4.0 with the ITER 3D model"*, Fus. Eng. Des. 82 (2007) 2861–2866

[8] Y. Wu, FDS Team, *"CAD-based Interface Programs for Fusion Neutron Transport Simulation"*, Fus. Eng. Des. 84 (2009) 1987-1992

[9] FENDL-2.1: Fusion Evaluated Nuclear Data Library ver2.1, (2004) https://www-nds.iaea.org/fendl21/

[10] FENDL-3.1d: Fusion Evaluated Nuclear Data Library ver.3.1d, (2018) https://wwwnds.iaea.org/fendl/

[11] D. Flammini, 2017 Generic DEMO MCNP model at 22.5 degree v1.3 (2019)

[12] F. Moro et al, Nuclear analysis of the Water-cooled lithium lead DEMO reactor, Fusion Engineering and Design 160 (2020) 111833

[13] F. Iannone et al., "MARCONI-FUSION: The new high performance computing facility for European nuclear fusion modelling", Fusion Eng. Des. 129 (2018) 354-358

[14] W. Mosher et al. ADVANTG - An Automated Variance Reduction Parameter Generator, ORNL/TM 2013/416 Rev. 1. Technical report, Oak Ridge National Laboratory, 2015

[15] M. Fabbri, Á. Cubí, iWW-GVR: A tool to manipulate MCNP weight windows (WW) and to generate Global Variance Reduction (GVR) parameters
URL: https://github.com/Radiation-Transport/iWW-GVR

[16] ICRP, Conversion coefficients for use in radiological protection against external radiation. ICRP publication 74, Ann. ICRP 26 (3–4) (1996).

[17] M. Dentan and J.- L. Leray. Proposed Strategy for Electronics Exposed to Nuclear Radiations in ITER, ITER IDM Reference: ITER_D_QXPP97, 2015

[18] V. Voitsenya Diagnostic first mirrors for burning plasma experiments, Review of Scientific Instruments 72, 475 (2001)

[19] P. Mertens et al. On the use of rhodium mirrors for optical diagnostics in ITER, Fusion Engineering and Design 146-B (2019) 2514-2518

[20] J.-Ch. Sublet et al. FISPACT-II: An Advanced Simulation System for Activation, Transmutation and Material Modelling, Nuclear Data Sheets 139 (2017) 77-137

[21] A. J. M. Plompen et al. The joint evaluated fission and fusion nuclear data library, JEFF-3.3, The European Physical Journal A, 56:181(2020)

[22] J. Blachot, Nuclear Data Sheets for A=104*, Nuclear Data Sheets 108 (2007) 2035–2172

[23] A. Serikov et al., "Neutron Induced Radiation Effects in Materials of ITER Diagnostics," 7th International Workshop on Plasma Material Interaction Facilities for

Fusion Research (PMIF 2019), October 22-25, 2019, La Jolla, USA, DOI: 10.13140/RG.2.2.21073.68964

[24] X. Huang and M. Kang, Nuclear Data Sheets for A=198*, Nuclear Data Sheets 133 (2016) 221-416

[25] G. Federici et al. DEMO design activity in Europe: Progress and updates, Fusion Engineering and Design 136-A (2018) 729-741